Mechanical and structural properties of radiation-damaged allanite-(Ce) and the effects of thermal annealing

Claudia E. Reissner[1,*], Ulrich Bismayer[2], Daniel Kern[3], Michael Reissner[3], Sulgiye Park[4], Jiaming Zhang[4], Rodney C. Ewing[4], Anna Shelyug[5], Alexandra Navrotsky[5], Carsten Paulmann[2,6], Radek Škoda[7], Lee A. Groat[8], Herbert Pöllmann[1] and Tobias Beirau[1,*]

[1]Institute of Geosciences and Geography, Martin-Luther-University Halle-Wittenberg, 06120 Halle (Saale), Germany

[2]Department of Earth Sciences, University of Hamburg, 20146 Hamburg, Germany

[3]Institute of Solid State Physics, TU Wien, 1040 Vienna, Austria

[4]Department of Geological Sciences, Stanford University, Stanford, CA 94305-2115, U.S.A.

[5]Peter A. Rock Thermochemistry Laboratory & NEAT ORU, University of California Davis, Davis, CA 95616, U.S.A.

[6]HASYLAB, DESY, 22603 Hamburg, Germany

[7]Institute of Geological Sciences, Faculty of Science, Masaryk University, 611 37 Brno, Czech Republic

[8]Department of Earth, Ocean and Atmospheric Sciences, University of British Columbia, Vancouver, BC V6T 1Z4, Canada

*Corresponding authors: claudia.reissner@geo.uni-halle.de, +49/345/5528247; and tobias.beirau@geo.uni-halle.de, +49/345/5526123

Abstract

The onset of thermally induced, heterogeneous structural reorganization of highly radiation-damaged allanite-(Ce) begins at temperatures below 700 K. Three strongly disordered allanite samples (S74 20414: ~0.55 wt% ThO_2, 22.1 wt% REE oxides, and maximum radiation dose 3.5×10^{18} α-decay/g; LB-1: 1.18 wt% ThO_2, 19.4 wt% REE oxides, and maximum radiation dose 2.0×10^{19} α-decay/g; R1: ~1.6 wt% ThO_2, 19.7 wt% REE oxides, and maximum radiation dose 2.6×10^{18} α-decay/g) were step-wise annealed to 1000 K in air. Using orientation-dependent nanoindentation, synchrotron single-crystal X-ray diffraction (synchrotron XRD), X-ray powder diffraction (powder XRD), differential scanning calorimetry and thermogravimetric analysis (DSC/TG), mass spectrometry (MS), ^{57}Fe Mössbauer spectroscopy and high-resolution transmission electron microscopy (HRTEM), a comprehensive understanding of the structural processes involved in the annealing was obtained. As a result of the overall increasing structural order, a general increase of hardness (pristine samples: 8.2-9.3 GPa, after annealing at 1000 K: 10.2-12 GPa) and elastic modulus (pristine samples: 115-127 GPa, after annealing at 1000 K: 126-137 GPa) occurred. The initially heterogeneous recrystallization process is accompanied by oxidation of iron, the related loss of hydrogen and induced stress fields in the bulk material, which cause internal and surface cracking after step-wise annealing from 800-1000 K. HRTEM imaging of the pristine material shows preserved nanometer-sized crystalline domains embedded in the amorphous matrix, despite the high degree of structural

40   damage. The results show that hardness and elastic modulus are sensitive indicators for the structural
41   reorganization process.
42
43   **Keywords**
44

59

60   **Introduction**
61

62   Allanite has a general formula $^{A1}(Ca)^{A2}(REE)^{M1,M2}(Al)_2^{M3}(Fe^{2+})[SiO_4][Si_2O_7]O(OH)$ and belongs to the allanite
63   group of the epidote-supergroup (Armbruster et al. 2006, Bonazzi et al. 2009, Mills et al. 2009). Allanite can have
64   a rare earth element (REE) oxide content of up to 26 wt% (Harlov et al. 2002) and therefore, has been historically
65   mined for rare earth elements (*e.g.*, Ehlmann et al. 1964, Maas et al. 1987). Furthermore, allanite has been used
66   for geochronological dating (*e.g.* Catlos et al. 2000, Romer & Siegesmund 2003, Gregory et al. 2007, McFarlane
67   2016, Fu et al. 2017). If Ce is the dominant REE it is designated as allanite-(Ce) (according to the Levinson rule)
68   with composition $Ca(Ce,La,Ca)(Fe^{2+},Fe^{3+})(Al,Fe^{3+})Al(Si_2O_7)(SiO_4)O(OH)$ (Ercit 2002, Armbruster et al. 2006).
69   The crystal structure is monoclinic ($P2_1/m$), composed of a framework of two types of edge-sharing octahedral
70   chains (single M1 octrahedra chain and a multiple chain of M2 and peripheral M3 octahedra) cross-linked by SiO_4
71   and Si_2O_7 groups (Fig. 1) (Dollase 1973). The M1 site can be occupied by Al, Fe, Mg, Mn, Ti, Cr, and V, and the
72   M3 site by Fe, Mn, Mg, Al, Cu, Cr, and V, whereas the M2 site is usually only occupied by Al. The M3 octahedra's
73   corner links to the Si sites from polyhedral (A1 and A2) positions, which host Ca, Mn, and Na (A1), and Ce or
74   other lanthanides, as well as actinides such as U and Th or other cations (*e.g.*, Sr, Pb, and Cd) (A2) (Ercit 2002).
75   A proton is attached to the O10 atom of the M2 octahedron by covalent bonding (Dollase 1973).
76   The incorporated U and/or Th cause the allanite to become amorphous or metamict due to alpha-decay events.
77   During the alpha-decay an α-particle ($^4_2He^{2+}$ nucleus) and a heavy recoil nucleus are generated (Ewing et al. 2000).
78   The smaller α-particle has higher energies (~4.5–5.8 MeV for actinides) and a longer trajectory of ~15–22 µm
79   compared to the recoil nucleus. Along its trajectory the α-particle's energy is dissipated by electronic excitations,
80   displacing several hundreds of atoms by the end of its path. The heavier recoil nucleus, despite having a lower

81   kinetic energy (70–100 keV) and a shorter trajectory of ~30 – 40 nm, displaces several thousand atoms, creating a

82   collision cascade mostly by elastic collisions (Ewing 2011).

83   Up to now, very little is known about the response of the mechanical properties of different mineral structures to

84   α-decay induced damage. Mechanical softening as a function of increasing radiation dose was observed by

85   Chakoumakos et al. (1991) and Beirau et al. (2016a, 2018) in zircon. Annealing of radiation-damaged Ti-Nb-Ta

86   oxides leads to an increase of the hardness during structural reorganization (Ewing 1973). Partially amorphous

87   titanite shows an initial softening and subsequent increase of hardness and elastic moduli due to thermal treatment

88   (Salje et al. 2011, Beirau et al. 2016b). In this study, the mineral allanite-(Ce), which can incorporate up to 5 wt%

89   ThO_2, (Exley 1980, Gieré & Sorensen 2004), was chosen because it contains structural OH^- groups. Their general

90   influence is of major interest as OH is assumed to act as a catalyst for thermally induced recrystallization processes

91   in radiation-damaged minerals (Zhang et al. 2000).

92   The recrystallization behavior of radiation-damaged allanite was studied using powder XRD by Janeczek & Eby

93   (1993). They observed the first stage of thermally induced reorganization, related to partial recrystallization of the

94   amorphous compound, in the temperature interval of 773 to 873 K. Čobić et al. (2010) found that recrystallization

95   in air resulted in partial recovery of allanite-(Ce) at 923 K, followed by structural decomposition at higher

96   temperatures, whereas hydrothermal treatment leads to an earlier and quicker reorganization process without

97   evidence of structural decomposition. Annealing experiments in air showed a significant increase in the unit-cell

98   parameter along the *c* axis at 873 K – 1073 K due to the loss of H^+ during $Fe^{2+} \rightarrow Fe^{3+}$ oxidation (Bonazzi &

99   Menchetti 1994). Vance and Routcliffe (1976) obtained a diffuse Laue pattern, showing no sharp spots, from one

100   heavily damaged allanite after annealing at 673 K, while two other samples showed no such behavior up to

101   annealing temperatures of 1073 K.

102   The purpose of this study is to investigate how the mechanical properties (*i.e.*, elastic modulus and hardness) of

103   radiation-damaged allanite-(Ce) are affected by a step-wise thermal treatment. To avoid the reported

104   decomposition of allanite at higher temperatures (*e.g.*, Janeczek & Eby 1993, Čobić et al. 2010), the maximum

105   temperature investigated was limited to 1000 K. The onset of thermally induced, heterogeneous structural

106   reorganization was revealed to occur at temperatures between 500 and 700 K, as found by nanoindentation,

107   synchrotron single-crystal XRD, and DSC measurements. In addition, mass spectrometry and ^{57}Fe Mössbauer

108   spectroscopy enabled us to follow the coupled processes of iron oxidation and dehydration.

109

110   **Samples and Methods**

111

112   **Allanite-(Ce) samples**

113

114   Three allanite-(Ce) samples (S74 20414, LB-1 and R1) from different locations and with distinct ThO_2 contents

115   and ages were investigated (see Table 1), to enable a general statement on the recrystallization behavior of allanite.

116   All crystals are opaque, black to black-brown, and have a vitreous luster. From each locality one larger sample

117   was fragmented, while the fragments were thermally annealed individually.

118   Sample S74 20414 is from Hitterö Island in Norway. It has the highest REE content of 22 wt% of which 11.47

119   wt% is Ce_2O_3. It also has the lowest ThO_2 content of only 0.55 wt% (see Table 2). Hetherington et al. (2008) dated

120   xenotimes in the surrounding pegmatitic rocks using U-Pb-Th methods and obtained an age of 923 ± 8 Ma.

121 Sample LB-1 originates from pegmatitic rocks in Holmtjärn, Sweden. The total REE content is about 20 wt%,

122 however, only 7.06 wt% of this is Ce_2O_3. The ThO_2 content is also slightly lower than in sample R1, 1.18 wt%

123 (see Table 2), but with an age of 1520 Ma as determined using U-Pb-Th isotopes by Welin & Blomqvist (1964).

124 Sample R1 came from the collection of the Fersman Mineralogical Museum of the Russian Academy of Science

125 in Moscow, Russian Federation. It is from Savvushka, Altai, Russian Federation. The R1 sample contains almost

126 20 wt% rare earth element oxides including 10.4 wt% Ce_2O_3 and has an actinide oxide content of 1.59 wt% ThO_2

127 (see Table 2). The rocks in the area of the locality (northern Altai Mountains) have been dated to 243.5 ± 2.1 Ma

128 using Rb-Sr isochrones from zircon (Vladimirov et al. 1997) and by $^{40}Ar/^{39}Ar$ dating on biotite to 244 ± 1.1 Ma

129 (Gavryushkina et al. 2017).

130 Using the ages of 923 Ma for S74 20414, 1520 Ma for LB-1, and 244 Ma for R1, maximum life-time alpha-decay

131 event doses (D) of 3.5×10^{18} α-decay/g, 2.0×10^{19} α-decay/g, and 2.6×10^{18} α-decay/g, respectively, can be

132 calculated using

133

$$D = 6 \frac{c_{Th} \cdot N_A}{M_{232} \cdot 10^6} (e^{\lambda_{232} t} - 1) \tag{1}$$

135

136 with c_{Th} being the thorium concentration, N_A the Avogadro-constant, M_{232} the mass of the ^{232}Th isotope, λ_{232}=4.93

137 $\times 10^{-11}$ y^{-1} the decay constant of ^{232}Th (from Firestone & Shirley 1996), and t the integration time (after Nasdala

138 et al. 2001). As the uranium content was below detection limit, the doses were calculated only on the basis of the

139 thorium content.

140

Chemical analysis

142

143 Electron microprobe measurements were completed on a CAMECA Camebax microbeam SX SEM system with

144 an acceleration voltage of 15 keV, a probe current of 20 nA and a beam size of 3 μm. Five to ten points distributed

145 over one grain per sample were measured and the average was formed. A ZAF correction was used for intensity-

146 mass correlation. An X-PHI (Merlet 1994) routine was used for matrix correction. Standards used were almandine

147 (Fe-Kα), spessartine (Mn-Kα), $NdPO_4$ (Nd-Lβ), $PrPO_4$ (Pr-Lβ), $LaPO_4$ (La-Lα), $CePO_4$ (Ce-Lα), anatase (Ti-Kα),

148 sanidine (Si-Kα, Al-Kα), Mg_2SiO_4 (Mg-Kα), YAG (Y-Lα), $ScVO_4$ (Sc-Kα), wollastonite (Ca-Kα), $CaTh(PO_4)_2$

149 (Th-Mα), albite (Na-Kα), $SmPO_4$ (Sm-Lβ), fluorapatite (P-Kα), U (U-Mβ), topaz (F-Kα), $GdPO_4$ (Gd-Lβ), $TbPO_4$

150 (Tb-Lα), $DyPO_4$ (Dy-Lβ), $HoPO_4$ (Ho-Lβ), $ErPO_4$ (Er-Lα), zircon (Zr-Lα), $EuPO_4$ (Eu-Lβ), and vanadinite (Pb-

151 Mα, Cl-Kα). Empirically determined correction factors were applied for F-Ce interference and other inter-REE

152 interferences (see Škoda et al. 2015). These new results improve on the previous sample characterization of allanite

153 R1 by Beirau et al. (2011).

154

Synchrotron single-crystal X-ray diffraction

156

157 Synchrotron single-crystal XRD measurements were carried out at beamline F1 (HASYLAB/DESY) on sample

158 R1 using a kappa diffractometer equipped with a MarCCD165 detector. The sample-to-detector distance was 60

159 mm and the wavelength 0.71 Å. Progressive annealing studies were done with a N_2 gas-stream heating device.

160 The annealing time was set to 15 min for all temperatures, which was already sufficient to show early

161 recrystallization. Ten grains with diameters of < 0.1 mm were prepared in quartz-glass capillaries and fixed with

162   quartz-glass wool. Depending on the initial degree of structural damage and increasing recrystallization effects

163   during annealing, step width and exposure times were varied between 0.5° to 0.1° and 20.0 s to 2.0 s, respectively.

164   For temperature-dependent analysis, the raw data were rescaled with respect to the primary beam intensity and

165   varying exposure times (Paulmann et al. 2001). Corrections for external scattering were performed by averaging

166   a range of background frames and subtracting the resulting background scattering from the scaled raw data scans.

167   For each reflection an individual box was defined where the outer rim of the box was averaged as a background

168   signal, excluding every pixel with intensities larger than 3σ. This background-intensity was then subtracted from

169   the total intensity in the box thus yielding the intensity of the reflex in the frame. Through these peaks rocking

170   curves were placed (see Inset in Fig. 2). To fit those curves a Lorentz-function was used. After each annealing step

171   the samples were cooled to room temperature before measuring.

172

173   **Mössbauer spectroscopy**

174

175   ^{57}Fe Mössbauer measurements were performed in standard transmission geometry on powdered samples in

176   constant acceleration mode. The source was a 19 mCi ^{57}CoRh foil. Approximately 100 mg of each sample were

177   ground in an agate mortar to a fine powder, which was glued in a thin layer on a piece of paper filling a circle of

178   ca. 1 inch. After the measurement of the pristine sample, the glue was dissolved in acetone and the clean powder

179   was heated within 30 min up to the first annealing temperature (700 K) where it was held for 1 h. Afterwards it

180   was removed from the oven to cool down to ambient conditions. The thus annealed powder was glued again on a

181   piece of paper and measured at room temperature. This intermediate annealing was repeated at 800 K, 900 K, and

182   1000 K for each of the three samples. For the analysis of the obtained spectra the full Hamiltonian was solved.

183   Sample thickness was taken into account using the approximations given by Mørup and Both (1975).

184

185   **X-ray powder diffraction**

186

187   Powder XRD patterns were recorded using a Panalytical X'Pert[3] powder diffractometer with Bragg–Brentano

188   geometry, a sample spinner, and Cu-Kα radiation, operating at 45 kV with a current of 40 mA, a step-size of 0.01°

189   2θ, and a counting time of 150 s per step. The samples were ground in an agate mortar to a fine powder and step-

190   wise annealed for 1 h in air at temperatures of 500, 600, 700, 800, 900, 950 and 1000 K and measured at room

191   temperature after each annealing step.

192

193   **Transmission electron microscopy**

194

195   High-resolution imaging was done using a FEI Tecnai G2 F20 X-TWIN transmission electron microscope (TEM).

196   The pristine samples were crushed to a fine powder, which was then dispersed in deionized water and deposited

197   on a holey carbon-coated copper TEM grid. Images were collected using bright field mode at 200 kV. The high-

198   resolution images were analyzed using a Gatan Digital Micrograph.

199

200   **Nanoindentation**

201

The mechanical properties of bulk allanite-(Ce) samples (cut into cuboids of sizes: S74 20414: ~2×1×0.5 cm, LB-1: ~2×1×1 cm, and R1: ~3×1×1 cm) were measured using a Nanomechanics iNano nanoindenter equipped with a diamond Berkovich indenter tip, operating in the continuous stiffness mode (CSM). The indentations were made using a constant nominal strain rate of 0.2 s^{-1}. Using CSM, the sample stiffness (S) is measured continuously in the course of the loading process of the indenter (see Li & Bhushan 2002; Oliver & Pharr 2004). A small dynamic oscillation is imposed on the force or displacement signal, and the amplitude and phase of the corresponding signal is measured with a frequency-specific amplifier. The orientation-dependent measurements were performed on polished $(00\bar{1})$ and $(0\bar{1}0)$ planes of the R1 sample. Indentations on sample LB-1 were done on the $(1\bar{1}2)$ plane. Sample S74 20414 was unoriented. Various indents distributed over the entire sample surfaces (to ensure significant average results) were made on the pristine samples and after each annealing step. The instrument software calculated the hardness (H) and the elastic modulus (E) during the loading process according to Oliver & Pharr (1992) with

$$H = \frac{P}{A} \tag{2}$$

where P is the imposed load and A the projected contact area between the indenter and the sample determined from the shape of the indenter and using the Oliver and Pharr method (Joslin & Oliver 1990; Oliver & Pharr 2004). The measured contact stiffness (S) is related to the elastic properties of both the sample and indenter and the contact area through (Sneddon 1965)

$$S = \beta \frac{2}{\sqrt{\pi}} E_r \sqrt{A} \tag{3}$$

where β is a constant depending on the indenter geometry (for Berkovich geometry β = 1.05) (Oliver and Pharr 2004) and E_r is the reduced modulus given by

$$\frac{1}{E_r} = \frac{(1-v_i^2)}{E_i} + \frac{(1-v^2)}{E} \tag{4}$$

where E_i and v_i are elastic modulus and Poisson´s ratio of the indenter, respectively (for the diamond indenter E_i = 1141 GPa and v_i = 0.07) and E and v are the elastic properties of the sample. E_r considers that elastic displacement takes place in the sample and in the indenter (Oliver & Pharr 2004). Fused silica was used as a reference material to calibrate the indenter. The H and E values shown in this study are averages from indentation depths of 150 to 250 nm. A Poisson´s ratio of 0.18 has been used for all samples. The samples were step-wise annealed in air for 1 h at the chosen temperatures of 500, 700, 800, 900 and 1000 K. After each annealing step, they were cooled to room temperature before measuring.

Thermal and evolved gas analyses

The simultaneous DSC/TG (differential scanning calorimetry and thermogravimetry) analysis was performed with a Netzsch STA 449 C instrument. The pristine samples were ground into a fine powder of about 20 mg and annealed in a Pt pan to 1000 K in air with a heating rate of 10 K/min. Mass spectrometry (MS) to determine the evolved gases from room temperature to 1000 K was done using a QMS 403D Aeolos Netzsch instrument.

Results and discussion

Pristine radiation-damaged allanite-(Ce)

242 Electron microprobe analysis revealed a relatively homogeneous chemical composition for allanite-(Ce) sample
243 S74 20414, while samples LB-1 and R1 show small heterogeneities in their REE and Fe distribution (Table 2 and
244 supplementary material). Initial Fe^{3+}/Fe^{2+} ratios of 27:73 (S74 20414), 47:53 (LB-1), and 50:50 (R1), were
245 measured with Mössbauer spectroscopy (see Table 3). In Figure 3 the Mössbauer spectra of the pristine samples
246 and after step-wise annealing are shown. According to the ideal structure of allanite, Fe occupies the
247 crystallographic sites M1 and M3. On both sites, Fe can be incorporated as 2+ or 3+. Therefore, four different
248 subspectra for the four Fe species are expected to be present, which add up to the measured spectrum. Each
249 subspectrum is characterized by a doublet, indicating that the Fe atoms are nonmagnetic, with characteristic values
250 for center shift and quadrupole splitting. The relative intensities of the different subspectra correspond to the
251 number of different Fe atoms. The result of such a fit is not fully satisfying, because there are deviations of the
252 calculated spectra from the measured ones. This is not surprising, because due to the rather high α-doses the
253 structure is heavily disturbed. Whereas well crystallized allanite spectra show four sharp peaks, the concrete
254 spectra show only three rather broad peaks with decreasing intensity, going from the negative to the positive
255 velocity range. For sample S74 20414 the intensity of the middle peak (Fig. 3b, peak 2) is less pronounced then
256 for the other two samples (Fig. 3a and c). A similar three peak shape of the Mössbauer spectrum was observed by
257 Malczewsik & Grabias (2008) for an allanite (ALL3) from Franklin and Sussex County, New Jersey, which had
258 absorbed a rather high α-dose. To explain their spectrum they added another two subspectra corresponding to a
259 second M3 site with slightly different hyperfine parameters, due to different distortion of the M3 octahedra
260 (Malczewski & Grabias 2008). This new M3 site can also be occupied by both Fe^{2+} and Fe^{3+}, leading to two further
261 subspectra. A fit according to this model gives better coincidence between the calculated and measured spectra.
262 Concerning the amount and ratio of Fe^{2+} and Fe^{3+}, both fits – with four and six subspectra - give within the error
263 (see Table 3) the same results. Therefore, in Fig. 3 only the calculated spectra obtained with the six subspectra fits
264 are shown. The hyperfine parameters of the pristine samples obtained by the fit are very similar to those obtained
265 for the ALL3 sample by Malkczewski & Grabias (2008).

266 The high degree of long-range structural disorder due to radiation-damage caused by incorporated ThO_2 is
267 indicated by very broad amorphous background features in powder XRD patterns (~25-35° 2θ) of the pristine
268 samples (Fig. 4). Nevertheless, a broadened weak allanite Bragg signal can be detected between ~30-31° 2θ in all
269 three samples (cited as $(\bar{1}13)$ by Čobić et al. 2010, also observed by Janeczek & Eby 1993, and Hoshino et al.
270 2005). This is in excellent agreement with HRTEM showing an overall amorphous matrix with small preserved
271 crystalline domains (Fig. 5) which function as seed crystals leading to a heterogeneous recrystallization process
272 (discussed in the next section). Synchrotron single-crystal XRD measurements of sample R1 also indicate an
273 initially highly disordered structure, showing only a few weak and broad Bragg signals (see example in Fig. 2).
274 Sample LB-1 has the highest degree of structural order of all investigated samples as it shows the most preserved
275 Bragg maxima according to powder XRD (Fig. 4). This is confirmed by the Mössbauer results, as the FWHM
276 (Full Width at Half Maximum) of the peaks of the subspectra of the pristine samples is smallest for sample LB-1.
277 The calculated maximum radiation dose (Table 1) would indicate this sample to have the least structural order of
278 all three samples, which leads to the assumption that allanite LB-1 has experienced an event that led to its (partial)
279 recrystallization at some point. Such could be a geological event that leads to higher temperatures in the area like
280 a granite intrusion (Ödman 1939).

281 No orientation dependence for loading perpendicular to the $(00\bar{1})$ and $(0\bar{1}0)$ crystallographic planes of sample
282 R1 of the indentation hardness (9.3 ± 0.2 GPa and 9.3 ± 0.3 GPa, respectively) and elastic modulus (127.0 ±1.6

283 GPa and 127.2 ± 3.2 GPa, respectively) could be detected (Tables 4 and 5, Fig. 6). This is the result of

284 amorphization that renders the mechanical properties isotropic, which has also been observed for natural, highly

285 radiation-damaged zircon (Beirau et al. 2016a). The indentation hardness of samples LB-1 and S74 20414 was

286 found to be 8.8 ± 0.5 GPa and 8.2 ± 0.1 GPa, respectively, and the elastic modulus 123.2 ± 5.7 GPa and 115.3 ±

287 2.1 GPa, respectively (Tables 4 and 5). Sample R1 shows the highest hardness and elastic modulus values of the

288 three investigated samples which is in agreement with the fact that it has experienced the lowest radiation dose

289 (Table 1). However, as sample LB-1 showed the highest structural order in the powder XRD patterns (Fig. 4)

290 indicating less structural damage (see above), but with H and E values close to R1 (Tables 4 and 5, Fig. 6).

291 Therefore, influences from differences in the chemical composition (Table 3) cannot be excluded.

292

293 **Effect of thermal annealing in air**

294

295 Mass spectrometry indicated an increase of OH/H_2O in the analyzed air gas stream during annealing of sample R1

296 in the region of ~350 - 525 K (maximum ~400 K) (Fig. 7b) that is probably due to the loss of water adhering to

297 the surface at these lower annealing temperatures. This increase is only slightly visible for sample LB-1 (Fig. 8b)

298 and not at all for sample S74 20414 (Fig. 9b). Above ~475 K the onset of a very broad exothermic process is

299 visible in the DSC signals of all three samples, accompanied by a steady slight weight loss (Figs. 7,8 and 9a). This

300 is in good agreement with the synchrotron XRD results of several analyzed grains of sample R1. They show an

301 increase of the integrated intensity and decrease of the FWHM of the exemplary Bragg maxima (231) (chosen due

302 to his initially sufficient intensity/background ratio) after step-wise annealing > 500 K (see exemplary Fig. 2). This

303 indicates the healing of defects and an increase in grain size, hence the reestablishment of long-range order in the

304 system leading to smaller FWHM values. Not all grains, from the same sample, investigated by synchrotron XRD,

305 showed these early steps of structural reestablishment. Heterogeneity of the degree of structural disorder in the

306 fragments of R1 was also indicated by differences in peak intensities and FWHM. This heterogeneity seems to be

307 very local, as no effect on a larger scale could be observed. In a similar temperature region (~575–610 K) all DSC

308 signals show a sharper maximum, while TG analysis shows a stronger mass loss (Figs. 7,8 and 9a). At these

309 temperatures, the MS signal indicates a small CO_2 loss (Figs. 7,8 and 9b). In samples LB-1 and S74 20414 an

310 additional, larger peak at ~850–1000 K can be observed. However, in sample R1 only the smaller peak is present

311 at temperatures of ~500–700 K and none at higher temperatures. The powder XRD pattern of sample S74 20414

312 shows a Bragg signal at 29° 2θ that can be attributed to calcite, which vanishes after annealing at temperatures of

313 900 K (Fig. 4a). Calcite inclusions in allanite have been described by Papunen and Lindsjö (1972), and the

314 temperature at which CO_2 is released (Figs. 8 and 9b) in these samples corresponds well to the collapse of

315 weathered calcite which starts thermal dissociation at around 875–975 K (Földvári 2011). DSC/TG and MS

316 measurements show the highest CO_2 loss in sample S74 20414 (Fig. 9b), with slightly fewer intensities in sample

317 LB-1 (Fig. 8b). Sample R1 shows comparably little loss in CO_2 (Fig. 7b). The OH and H_2O loss are highest in

318 sample LB-1, and least in sample R1 as discussed below in further detail (see Figs. 7, 8 and 9b).

319 The mechanical properties of all three samples provide evidence for structural reorganization after annealing at

320 700 K, showing a noticeable increase of the elastic modulus to 122.4 ± 1.8 GPa, 128.9 ± 6.8 GPa, 137.1 ± 2.0 GPa

321 and 131.1 ± 2.7 GPa for samples S74 20414, LB-1, R1 (00$\bar{1}$), and R1 (0$\bar{1}$0), respectively, as well as an increase

322 in hardness to 9.2 ± 0.1 GPa, 10.3 ± 0.7 GPa, 10.2 ± 0.2 GPa and 9.3 ± 0.3 GPa for samples S74 20414, LB-1, R1

323 (00$\bar{1}$), and R1 (0$\bar{1}$0), respectively (see Fig. 6, Tables 4, 5). The increase in hardness and modulus indicates an

increasing overall structural integrity and bond strengthening due to thermal treatment. The powder XRD measurements, more sensitive to long-range periodicity, show no clear evidence for this early recrystallization process. That is in good agreement with previous results (Janeczek & Eby 1993, Čobić et al 2010). One could also expect masking effects of higher amounts of more damaged material in the investigated powders, superimposing the signals from already recrystallizing, comparably small, less-damaged domains.

Starting at annealing temperatures of ~ 650 K an increase in hydrogen in the analyzed gas stream was detected by MS (measured as masses 17 and 18 which were assigned to OH and H_2O, respectively) with a maximum around 880 K (Figs. 7, 8 and 9b). This is accompanied by iron oxidation ($Fe^{2+} \rightarrow Fe^{3+}$) observed by Mössbauer spectroscopy, as with increasing annealing temperature the peak at the highest positive velocity (Fig. 2, peak 3) vanishes. Due to the position of this peak, it can be attributed to Fe^{2+} high spin. Starting with Fe^{2+}/Fe^{3+} ratios of 2.68, 1.11, and 1.00 for samples S74 20414, LB-1, and R1, respectively, the ratio decreased with increasing annealing temperature, reaching 0 for samples R1 and S74 20414 between 800 K and 900 K, whereas for sample LB-1 16.1% of Fe^{2+} was still present after annealing at 1000 K (Table 3). This oxidation is an increasingly strong endothermic process, visible in the DSC signal starting around ~ 700 K until ~ 1000 K when all Fe^{2+} is oxidized except for that in sample LB-1 (Figs. 7, 8 and 9a). One can expect this process to superimpose on the ongoing exothermic structural reorganization. These findings are in excellent agreement with the assumption that hydrogen loss serves as charge compensation for the iron oxidation (Dollase 1971; Bonazzi & Menchetti 1994) which has been reported to start > 673 K and be complete around 973 K for allanite (Dollase 1971; see also Gieré & Sorensen 2004).

Step-wise annealing above 900 K causes a sharpening of the ($\bar{1}13$) Bragg-reflex in the powder XRD patterns (Fig. 4). After annealing at 900 K the hardness and modulus of sample LB-1 show a further increase to 11.4 ± 0.8 GPa and 149.6 ± 9.5 GPa, respectively. Even higher values are seen after annealing at 1000 K with a hardness of 12.0 ± 0.9 GPa and an elastic modulus of 163.0 ± 12 GPa (Fig. 6, Tables 4, 5). This trend is not visible for samples S74 20414 and R1 (Fig. 6, Tables 4,5). The higher OH⁻ content of sample LB-1 could be the cause of the more rapid recrystallization and the stronger increases in hardness and modulus. Čobić et al. (2010) also found quicker recrystallization in allanite samples that were annealed under hydrothermal conditions. Furthermore, the induced interior stress caused by heterogeneous recrystallization and hydrogen loss leads to internal and surface cracking at higher temperatures (visible under the microscope and in the depth evolution of the mechanical properties). This hampers the precise determination of *H* and *E* values after step-wise annealing in the region of 800 up to 1000 K, as fracturing leads to a decrease of the mechanical properties (Walsh 1965). One can expect the mechanical properties to increase further with increasing overall crystallinity, but due to the internal failure of the material they become partially strongly disturbed, leading to larger errors. Nevertheless, despite the reducing effect of fracturing, an increase (LB-1) or at least an overall plateau-like behavior (R1 and S74 20414) is visible for *H* and *E* at higher annealing temperatures. However, the difference in chemical composition, (e.g., Ce_2O_3 makes up over half the REE content in samples S74 20414 and R1 and only a little over a third in sample LB-1 (Table 2 and supplementary material)), might also have an influence on the recrystallization behavior, as well as the difference in the initial degree of disorder.

Conclusions

Thermal treatment of radiation-damaged allanite-(Ce) leads to heterogeneous recrystallization, due to the presence of less-damaged domains in the material. The recrystallization process starts around 550 K, as seen in the synchrotron data, and goes on continuously. Low-temperature annealing at 700 K leads to an increase in the mechanical properties of about 5% in the elastic modulus and about 10% in the hardness in all investigated samples. This further indicates a restoration of long-range order in the structure due to the reorganization process. In the temperature region of ~ 700 to 1000 K the structural Fe^{2+} oxidizes in air, which is coupled to the loss of hydrogen. The revealed adverse effect of internal and surface cracking reaches a maximum after annealing at 900 K, when almost all Fe^{2+} is oxidized, and the most hydrogen is lost. The elastic modulus is more sensitive to fracturing than hardness. The initial maximum alpha-radiation dose (as calculated according to Equ. 1, see Table 1) as well as the assumed degree of structural damage (as estimated from powder XRD, see Fig. 4) do not seem to correlate completely with the H and E order of the three samples. Although a comparison of samples R1 and S74 20414 show higher H and E values with higher structural order, sample LB-1, showing initially the highest degree of structural order, has intermediate E and H values compared to the other two samples. It is, therefore, assumed that differences in chemistry and/or orientation also have a noticeable impact. Nevertheless, despite their differences in chemistry, radiation damage and orientation, all three samples showed an increase in H and E at the same annealing temperature (700 K) thus indicating a similar behavior in the recrystallization offset. The higher OH^- content in sample LB-1 seems to act as a catalyst in the structural reorganization process, as assumed by Zhang et al. (2010) for zircon, leading to a stronger increase in the mechanical properties at higher temperatures (i.e. during the oxidation/dehydration process). In conclusion, the mechanical properties (E and H) are sensitive indicators of the degree of structural reorganization during the annealing process.

References

Armbruster T, Bonazzi P, Akasaka M, Bermanec V, Chopin C, Gieré R, Heuss-Assbichler S, Liebscher A, Menchetti S, Pan Y, Pasero M (2006) Recommended nomenclature of epidote-group minerals. Eur J Mineral 18:551–567. https://doi.org/10.1127/0935-1221/2006/0018-0551

Beirau T, Nix WD, Bismayer U, Boatner LA, Isaacson SG, Ewing RC (2016a) Anisotropic properties of zircon and the effect of radiation damage. Phys Chem Minerals 43:627–638. https://doi.org/10.1007/s00269-016-0822-9

Beirau T, Nix WD, Ewing RC, Pöllmann H, Salje EKH (2018) Radiation-damage-induced transitions in zircon: Percolation theory applied to hardness and elastic moduli as a function of density. Appl Phys Let 112:201901. https://doi.org/10.1063/1.5030626

Beirau T, Nix WD, Ewing RC, Schneider GA, Groat LA, Bismayer U (2016b) Mechanical properties of natural radiation-damaged titanite and temperature-induced structural reorganization: A nanoindentation and Raman spectroscopic study. Am Mineral 101:399–406. http://dx.doi.org/10.2138/am-2016-5433

Beirau T, Paulmann C, Bismayer U (2011) Recrystallization of metamict allanite. Mineral Mag 75(4):2393–2399. https://doi.org/10.1180/minmag.2011.075.4.2393

Bonazzi P, Holtstam D, Bindi L, Nysten P, Capitani GC (2009) Multi-analytical approach to solve the puzzle of an allanite-subgroup mineral from Kesebol, Västra Götaland, Sweden. Am Mineral 94:121–134. https://doi.org/10.2138/am.2009.2998

Bonazzi P, Menchetti S (1994) Structural variations induced by heat treatment in allanite and REE-bearing piemontite. Am Mineral 79:1176–1184.

405 Catlos EJ, Sorensen SS, Harrison TM (2000) Th-Pb ion-microprobe dating of allanite. Am Mineral 85:633–648.
406 https://doi.org/10.2138/am-2000-5-601

407 Chakoumakos BC, Oliver WC, Lumpkin GR, Ewing RC (1991) Hardness and elastic modulus of zircon as a
408 function of heavy-particle irradiation dose: I. In situ α-decay event damage. Radiat Eff Defect S 118(4):393–403.

409 Čobić A, Bermanec V, Tomašić N (2010) The hydrothermal recrystallization of metamict allanite-(Ce). Can
410 Mineral 48:513–521. https://doi.org/10.3749/canmin.48.3.513

411 Dollase WA (1971) Refinement of the crystal structure of epidote, allanite and hancockite. Am Mineral 56:447–
412 464.

413 Dollase WA (1973) Mössbauer spectra and iron distribution in the epidote-group minerals. Z Kristallogr 138:41–
414 63

415 Ehlmann AJ, Walper JL, Williams J (1964) A new, baringer hill-type, rare-earth pegmatite from the central mineral
416 region, Texas. Econ Geol 59:1348–1360. https://doi.org/10.2113/gsecongeo.59.7.1348

417 Ercit TS (2002) The mess that is "allanite". Can Mineral 40:1411–1419.
418 https://doi.org/10.2113/gscanmin.40.5.1411

419 Exley RA (1980) Microprobe studies of REE-rich accessory minerals: Implications for Skye Granite petrogenesis
420 and REE mobility in hydrothermal systems. Earth Planet Sc Lett 48:97–110

421 Ewing RC (1973) Vickers Hardness and Reflectance Determination for Metamict AB_2O_6-Type Rare Earth Ti-Nb-
422 Ta Oxides. Am Mineral 58:942–944

423 Ewing RC, Meldrum A, Wang LM, Wang SX (2000) Radiation-induced amorphization. Rev Mineral Geochem
424 39:319–361.

425 Ewing RC (2011) Actinides and radiation effects: impact on the back-end of the nuclear fuel cycle. Mineral Mag
426 75(4):2359–2377. https://doi.org/10.1180/minmag.2011.075.4.2359

427 Firestone RB, Shirley VS (1996) Table of isotopes 2. Wiley, New York

428 Földvári M (2011) Handbook of thermogravimetric system of minerals and its use in geological practice.
429 Occasional Papers of the Geological Institute of Hungary, Volume 213.

430 Fu Y, Sun X, Li D, Lin H, Lai C (2017) LA-ICP-MS U-Th-Pb Dating and Trace Element Geochemistry of Allanite:
431 Implications on the Different Skarn Metallogenesis between the Giant Beiya Au and Machangqing Cu-Mo-(Au)
432 Deposits in Yunnan, SW China. Minerals 7:251. https://doi.org/10.3390/min7120251

433 Gavryushkina OA, Travin AV, Kruk NN (2017) Duration of granitoid magmatism in peripheral parts of large
434 igneous provinces (Based on $^{40}Ar/^{39}Ar$ isotopic studies of Altai Permian-Triassic granitoids. Geodynamics
435 Tectonophysics 8(4):1035–1047. https://doi.org/10.5800/GT-2017-8-4-0331

436 Gieré R, Sorensen SS (2004) Allanite and Other REE-Rich Epidote-Group Minerals. Rev Mineral Geochem
437 56:431–493. https://doi.org/10.2138/gsrmg.56.1.431

438 Gregory CJ, Rubatto D, Allen CM, Williams IS, Hermann J, Ireland T (2007) Allanite micro-geochronology: A
439 LA-ICP-MS and SHRIMP U-Th-Pb study. Chem Geol 245:162–182.
440 https://doi.org/10.1016/j.chemgeo.2007.07.029

441 Harlov DE, Andersson UB, Förster H-J, Nyström JO, Dulski P, Broman C (2002) Apatite-monazite relations in
442 the Kiirunavaara magnetite-apatite ore, northern Sweden. Chem Geol 191:47–72. https://doi.org/10.1016/S0009-
443 2541(02)00148-1

444   Hetherington CJ, Jercinovic MJ, Williams ML, Mahan K (2008) Understanding geological processes with
445   xenotime: Composition, chronology, and a protocol for electron probe microanalysis. Chem Geol 254: 133–147.
446   https://doi.org/10.1016/j.chemgeo.2008.05.020

447   Hoshino M, Kimata M, Nishida N, Kyono A, Shimizu M, Takizawa S (2005) The chemistry of allanite from the
448   Daibosatsu Pass, Yamanashi, Japan. Mineral Mag 69(4):403–423. https://doi.org/10.1180/0026461056940259

449   Janeczek J, Eby RK (1993) Annealing of Radiation Damage in Allanite and Gadolinite. Phys Chem Minerals
450   19:343–356. https://doi.org/10.1007/BF00202971

451   Joslin DL, Oliver WC (1990) A new method for analyzing data from continuous depth-sensing microindentation
452   tests. J Mater Res 5(1):123–126

453   Kartashov PM, Ferraris G, Ivaldi G, Sokolova E, McCammon CA (2002) Ferriallanite-(Ce),
454    $CaCeFe^{3+}AlFe^{2+}(SiO_4)(Si_2O_7)O(OH)$, a new member of the epidote group: Description, X-ray and Mössbauer
455   study. Can Mineral 40:1641–1648

456   Li X, Bhushan B (2002) A review of nanoindentation continuous stiffness measurement technique and its
457   applications. Mater Charact 48:11–36. https://doi.org/10.1016/S1044-5803(02)00192-4

458   Maas R, McCulloch MT, Campbell IH (1987) Sm-Nd Isotope Systematics in Uranium-Rare Earth Element
459   Mineralization at the Mary Kathleen Uranium Mine, Queensland. Econ Geol 82:1805–1826.
460   https://doi.org/10.2113/gsecongeo.82.7.1805

461   Malczewski D, Grabias A (2008) 57Fe Mössbauer Spectroscopy of Radiation Damaged Allanites. Acta Phys Pol
462   A 114(6):1683–1690. https://doi.org/10.12693/APhysPolA.114.1683

463   McFarlane CRM (2016) Allanite U—Pb geochronology by 193 nm LA ICP-MS using NIST610 glass for external
464   calinration. Chem Geol 438:91–102. http://dx.doi.org/10.1016/j.chemgeo.2016.05.026

465   Merlet C (1994) An Accurate Computer Correction Program for Quantitative Electron Probe Microanalysis.
466   Microchim Acta 114/115:363–376

467   Mills SJ, Hatert F, Nickel EH, Ferraris G (2009) The standardisation of mineral group hierarchies: application to
468   recent nomenclature proposals. Eur J Mineral 21:1073–1080. https://doi.org/10.1127/0935-1221/2009/0021-1994

469   Mørup S, Both E (1975) Interpretation of Mössbauer spectra with broadened lines. Nuclear Instruments and
470   Methods 124(2): 445-448. https://doi.org/10.1016/0029-554X(75)90595-9

471   Nasdala L, Wenzel M, Vavra G, Irmer G, Wenzel T, Kober B (2001) Metamictisation of natural zircon:
472   accumulation versus thermal annealing of radioactivity-induced damage. Contrib Mineral Petrol 141:125–144.
473   http://dx.doi.org/10.1007/s004100000235

474   Ödman, OH (1939) The Gold-Copper-Arsenic Ore at Holmtjärn, Skellefte District, N. Sweden. Geol Foren Stock
475   For 61(1):91–111. http://dx.doi.org/10.1080/11035893909446035

476   Oliver WC, Pharr GM (1992) An improved technique for determining hardness and elastic modulus using load
477   and   displacement   sensing   indentation   experiments.   J   Mater   Res   7(6):1564–1583.
478   https://doi.org/10.1557/JMR.1992.1564

479   Oliver WC, Pharr GM (2004) Measurement of hardness and elastic modulus by instrumented indentation:
480   Advances   in   understanding   and   refinements   to   methodology.   J   Mater   Res   19(1):3–20.
481   https://doi.org/10.1557/jmr.2004.19.1.3

482   Papunen H, Lindsjö O (1972) Apatite, monazite and allanite: Three rare earth minerals from Korsnäs, Finland. Bul
483   Geol Soc Finl 44:123–129

484 Paulmann C, Kurtz R, Bismayer U (2001) Software development for studies of diffuse scattering using CCD-
485 detectors and synchrotron radiation sources. Nucl Instrum Meth A 467–468:1113–1116

486 Romer RL, Siegesmund S (2003) Why allanite may swindle about its true age. Contrib Mineral Petrol 146:297–
487 307. https://doi.org/10.1007/s00410-003-0494-6

488 Salje EKH, Safarik DJ, Lahley JC, Groat LA, Bismayer U (2011) Elastic softening of metamict titanite $CaTiSiO_5$:
489 Radiation damage and annealing

490 Škoda R, Plášil J, Jonsson E, Čopjaková R, Langhof J, Galiová MV (2015) Redefinition of thalénite-(Y) and
491 discredition of fluorthelénite-(Y): A reinvestigation of type material from the Österby pegmatite, Dalarna, Sweden,
492 and from additional localities. Mineral Mag 79(4):965–983. https://doi.org/10.1180/minmag.2015.079.4.07

493 Sneddon IN (1965) The relation between load and penetration in the axisymmetric buissinesq problem for a punch
494 of arbitrary profile. Int J Eng Sci 3:47–57. https://doi.org/10.1016/0020-7225(65)90019-4

495 Vance ER, Routcliffe P (1976) Heat treatment of some metamict allanites. Mineral Mag 40:521–523.

496 Vladimirov AG, Ponomareva AP, Shokalskii SP, Khalilov VA, Kostitsyn YA, Ponomarchuk VA, Rudney SN,
497 Vystavnoi SA, Kruk NN, Titov AV (1997) Late Paleozoic early Mesozoic granitoid magmatism in Altai.
498 Geologiya & Geofizika 38:715–729

499 Walsh JB (1965) The Effect of Cracks on the Uniaxial Elastic Compression. J Geophys Res 70(2):399–411

500 Welin E, Blomqvist G (1964) Age measurements on radioactive minerals from Sweden. Geol Foren Stock For
501 86(1):33–50. http://dx.doi.org/10.1080/11035897.1964.9626366

502 Zhang M, Salje EKH, Malcherek T, Bismayer U, Groat LA (2000) Dehydration of metamict titanite: an infrared
503 spectroscopic study. Can Mineral 38:119–130.

504

505 **Tables**

506

507 **Table 1** Location, age, wt% ThO_2 (from EMPA measurements, see Table 2) and dose (calculated after equation
508 1) for the investigated allanite-(Ce) samples. *Hetherington et al. (2008), **Welin & Blomqvist (1964),
509 ***Gavryushkina et al. (2017) and Vladimirov et al. (1997)

Sample	Location	Age [Ma]	wt% ThO_2	dose [α-decay/g]
S74 20414	Hitterö, Norway	923 ± 8 *	0.55	$3.5 \times 10^{18} \pm 4.5 \times 10^{15}$
LB-1	Holmtjärn, Sweden	1520 **	1.18	2.0×10^{19}
R1	Savvushka, Russia	244 ± 2.1***	1.59	$2.6 \times 10^{18} \pm 1.7 \times 10^{15}$

510

511 **Table 2** Electron microprobe compositions of allanite-(Ce) samples S74 20414, LB-1 and R1 (averaged over
512 five to ten points on each sample)

Oxide	wt%			Oxide	wt%		
	S74 20414	LB-1	R1		S74 20414	LB-1	R1
SiO_2	31.78	31.70	31.73	MnO	0.31	0.39	2.71
Al_2O_3	14.30	15.16	13.43	Cl	0.08	0.13	n.d.
FeO*	12.79	12.12	16.39	PbO	n.d.	0.07	n.d.
Ce_2O_3	11.47	7.06	10.38	Na_2O	n.d.	0.14	n.d.
CaO	10.94	11.15	10.96	Sm_2O_3	n.d.	1.73	n.d.
La_2O_3	7.00	2.63	5.73	Y_2O_3	n.d.	1.29	0.15
Nd_2O_3	2.88	4.97	2.20	Gd_2O_3	n.d.	1.19	n.d.
MgO	1.87	0.27	0.58	Sc_2O_3	n.d.	0.30	0.19
TiO_2	0.94	0.27	0.81	Dy_2O_3	n.d.	0.29	n.d.
Pr_2O_3	0.70	1.09	0.87	Tb_2O_3	n.d.	0.11	n.d.

| ThO₂ | 0.55 | 1.18 | 1.59 | Total | 95.61 | 93.24 | 97.72 |

513 *all Fe is assumed to be Fe^{2+} for the purpose of the chemical analysis

514

515 **Table 3** Change of amounts Fe^{2+} and Fe^{3+} with annealing temperature for samples S74 20414, LB-1, and R1
516 from Mössbauer spectroscopic analysis (see also Fig. 3)

Temperature [K]	S74 20414			LB-1			R1		
	Fe^{2+} [%]	Fe^{3+} [%]	Fe^{2+}/Fe^{3+}	Fe^{2+} [%]	Fe^{3+} [%]	Fe^{2+}/Fe^{3+}	Fe^{2+} [%]	Fe^{3+} [%]	Fe^{2+}/Fe^{3+}
pristine (300)	73±3	27±3	2.68	53±3	47±3	1.11	50±3	50±3	1.00
700	42±3	58±3	0.74	17±3	84±3	0.20	35±3	65±3	0.54
800	7±3	93±3	0.79	13±3	87±3	0.15	15±3	85±3	0.18
900	0	100	0	14±3	86±3	0.16	0	100	0
1000	0	100	0	16±3	84±3	0.19	0	100	0

517

518 **Table 4** Hardness values of allanite-(Ce) samples S74 20414, LB-1, and R1 (two orientations), after annealing at
519 different temperatures (all measurements were obtained at room temperature)

Temperature [K]	S74 20414	LB-1 ($1\bar{1}2$)	R1 ($00\bar{1}$)	R1 ($0\bar{1}0$)
	Hardness [GPa]	Hardness [GPa]	Hardness [GPa]	Hardness [GPa]
pristine (300)	8.19 ± 0.12	8.82 ± 0.46	9.29 ± 0.16	9.30 ± 0.30
500	8.29 ± 0.09	9.09 ± 0.51	9.24 ± 0.17	9.28 ± 0.27
700	9.21 ± 0.13	10.31 ± 0.71	10.24 ± 0.15	9.92 ± 0.26
800	9.81 ± 0.17	10.07 ± 0.39	10.86 ± 0.34	10.80 ± 0.35
900	9.91 ± 0.18	11.37 ± 0.78	11.27 ± 0.38	10.79 ± 0.27
1000	10.17 ± 0.32	12.02 ± 0.85	10.78 ± 0.36	10.83 ± 0.27

520

521 **Table 5** Elastic modulus values of allanite-(Ce) samples S74 20414, LB-1, and R1 (two orientations), after
522 annealing at different temperatures (all measurements were obtained at room temperature)

Temperature [K]	S74 20414	LB-1 ($1\bar{1}2$)	R1 ($00\bar{1}$)	R1 ($0\bar{1}0$)
	Elastic Modulus [GPa]	Elastic Modulus [GPa]	Elastic Modulus [GPa]	Elastic Modulus [GPa]
pristine (300)	115.3 ± 2.1	123.2 ± 5.7	127.0 ± 1.6	127.2 ± 3.2
500	116.0 ± 2.2	125.0 ± 5.1	126.5 ± 1.5	126.1 ± 2.8
700	122.4 ± 1.8	128.9 ± 6.8	137.1 ± 2.0	131.1 ± 2.7
800	124.0 ± 1.3	127.1 ± 4.5	135.3 ± 3.7	136.0 ± 3.4
900	126.3 ± 1.6	149.6 ± 9.5	134.2 ± 4.7	130.9 ± 3.6
1000	126.0 ± 3.9	163.0 ± 12.0	137.2 ± 5.8	133.6 ± 4.9

523

524 **Figure Captions**

525

526 **Fig. 1** Schematic representation of the ideal allanite-(Ce) structure. Data from Dollase (1971), visualized with
527 VESTA software. H atoms have been added after the image of Kartashov et al. (2002). Sites are described in the
528 Introduction.

529

530 **Fig. 2** Evolution of the integrated intensity [black circles] and FWHM [red boxes] of the (231) Bragg reflex from
531 synchrotron single-crystal X-ray diffraction as a function of annealing temperature from an exemplary grain of
532 sample R1. All measurements were obtained at room temperature. Error bars are within the size of the symbols.
533 The Inset shows the rocking curves before and after annealing at temperatures 573 K and 673 K.

534

Fig. 3 ^{57}Fe Mössbauer spectra of allanite-(Ce) samples a) S74 20414, b) LB-1, and c) R1 after step-wise annealing at the shown temperatures. All measurements were obtained at room temperature. The curves through the measurement points are the result of the fit with six different subspectra (for details see text). The numbering of the peaks is to simplify referencing in the text.

Fig. 4 Powder X-Ray diffractograms for allanite-(Ce) samples a) S74 20414, b) LB-1, and c) R1. The annealing temperatures are shown. All measurements were obtained at room temperature. Highlighted red regions indicate the position of the allanite reflexes. (indices from Čobić et al. (2010)). The signal at ~40–43 °2θ marked with a (*) represents two reflexes with indices (221) and ($\bar{2}$23) according to literature. The highlighted blue region marks the position of a calcite reflex in sample S74 20414 (appears at 500-600 K and disappears at 900 K).

Fig. 5 High resolution transmission electron microscope (HRTEM) images of preserved crystalline parts in amorphized matrix of radiation-damaged allanite-(Ce) samples a) S74 20414, b) LB-1, and c) R1. Insets show the corresponding FFT analyses.

Fig. 6 Evolution of the a) elastic modulus and b) hardness as a function of annealing temperature of allanite-(Ce) samples S74 20414 [pink diamonds], LB-1 [blue squares], and R1 on the ($00\bar{1}$) plane [red circles] and ($0\bar{1}0$) plane [black stars]. All measurements were obtained at room temperature.

Fig. 7 a) Differential scanning calorimetric (DSC) [black] and thermogravimetric (TG) [red] measurements of allanite-(Ce) sample R1 and b) mass spectrometry measurements (masses are assigned to: 12: C, 17: OH, 18: H_2O, and 44: CO_2).

Fig. 8 a) Differential scanning calorimetric (DSC) [black] and thermogravimetric (TG) [red] measurements of allanite-(Ce) sample LB-1 and b) mass spectrometry measurements (masses are assigned to: 12: C, 17: OH, 18: H_2O, and 44: CO_2).

Fig. 9 a) Differential scanning calorimetric (DSC) [black] and thermogravimetric (TG) [red] measurements of allanite-(Ce) sample S74 20414 and b) mass spectrometry measurements (masses are assigned to: 12: C, 17: OH, 18: H_2O, and 44: CO_2).
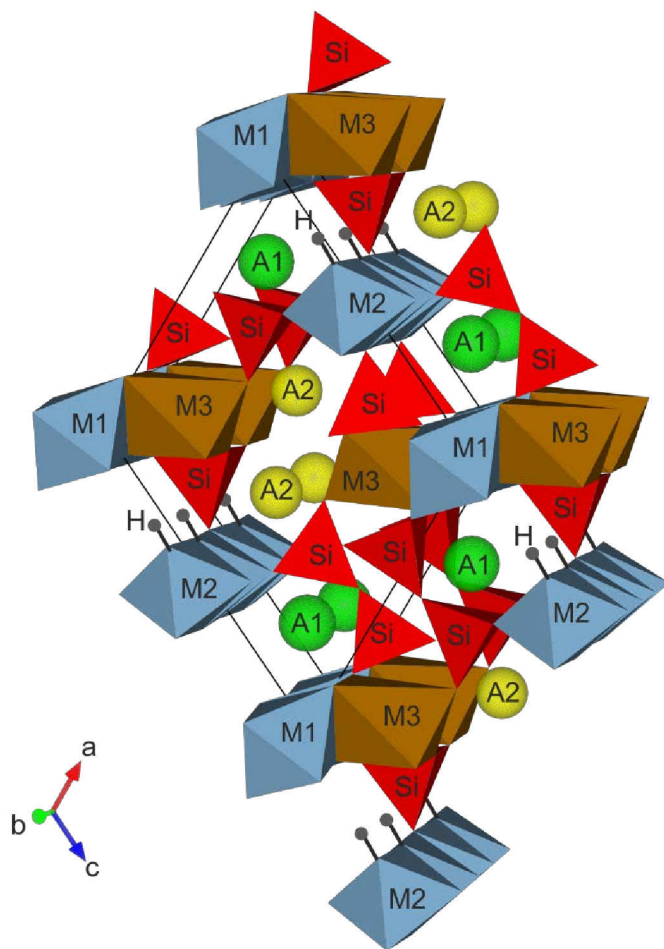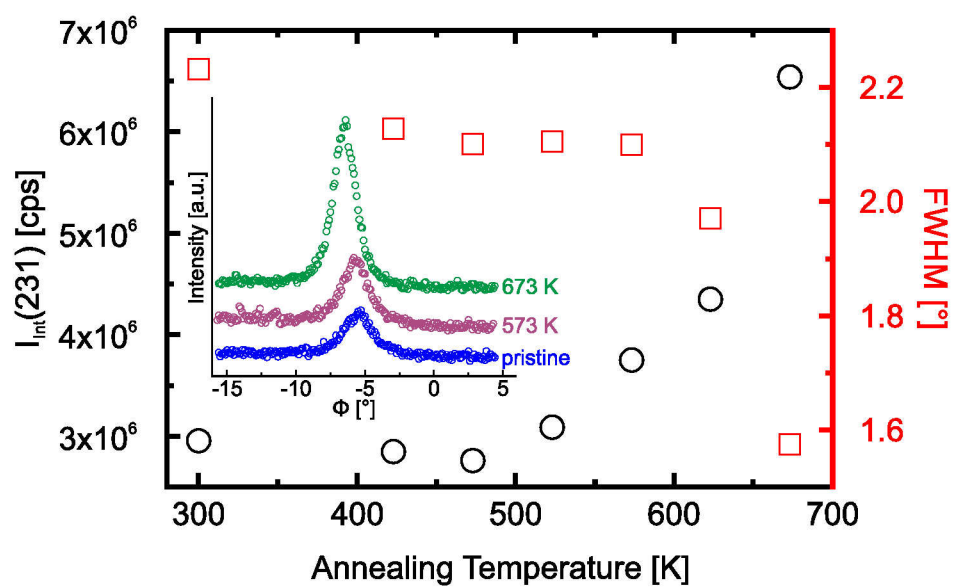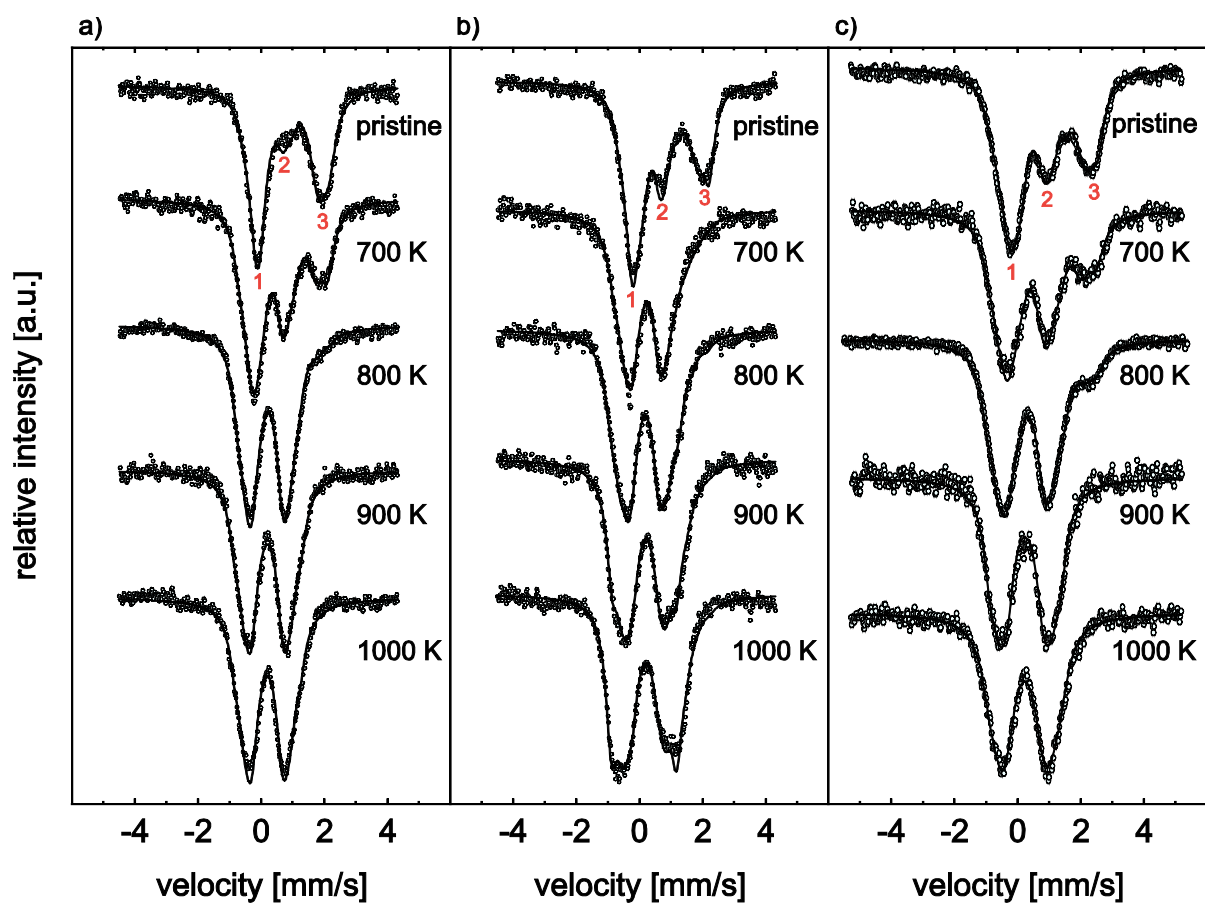
Figures

Fig. 1

570

571

572 Fig. 2

573

574

575

576 Fig. 3

577

578
579
580   Fig. 4
581

582

583

584   Fig. 5

585

586

587   Fig. 6

588

589

590

591   Fig. 7

592

593
594
595   Fig. 8
596

a)

b)

601